



FRAUNHOFER CHALMERS
RESEARCH CENTRE FOR INDUSTRIAL MATHEMATICS

FCC Technical Report 1/2022

Simulation Of Powder Coating

Models and methods developed in the Vinnova
funded project Quariapro

Tomas Johnson, Fredrik Edelvik



Introduction and background

Surface treatment is an important process, which impacts the properties, appearance, and durability of the treated object. There are many different treatments such as electroplating, electrocoating, powder coating, and spray coating. Powder coating is common in many industries from furniture manufacturing to truck cabs. Powder coating is usually applied by powder guns, but rotary powder bells also exist. The guns can be handheld, mounted on robots, or in reciprocator setups. A key aspect of powder coating is electrostatics; the powder is charged and attaches to the target object with electrostatic forces. In contrast to wet paint powder cannot be applied without electrostatics and does not stick permanently to the surface until after curing.

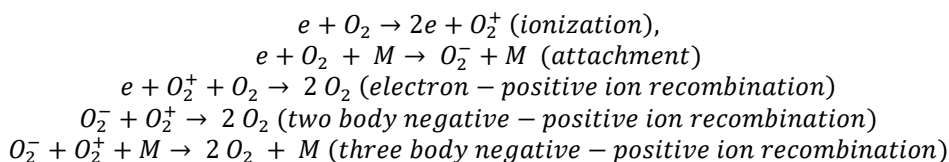
In this technical report we describe a theory and simulation model for powder coating and give an example for how this model can be used to generate input for industrial scale painting simulations aiming to compute the thickness profiles and size distributions on the target object. A complete industrial scale validation is outside the scope of this report. The models and methods presented herein have been developed in the Vinnova funded project Quariapro (*Optimize powder coating quality and material efficiency by connecting process actuators and a digital twin, Dnr 2019-05224*) and extend on previously performed research on the virtual paint shop for: wet paint (Edelvik, Mark, Karlsson, Johnson, & Carlson, 2017), sealing (Ingelsten, Mark, & Edelvik, 2019), and oven curing (Johnson, et al., 2022). The development of the models was supported by measurements performed by the project partner Fraunhofer IPA.

Simulation Models and Theory Overview

In this section we describe the models and methods used for the simulations. The description includes an overview of theory, models, and equations used to model powder coating. Several of the models need experimental input, i.e., they contain parameters that need to be fitted to data for the specific conditions and settings used for painting. Examples of experiments and how they are used as input to the models are described in the next section.

The modelling approach has three main stages consisting of: a resolved three species electrostatics model, detailed coupled electrostatics - fluid dynamics - particle dynamics simulation, and coarse coupled electrostatics - fluid dynamics - particle dynamics coating simulation.

In powder coating an electric current is discharged from a thin needle inside the powder gun, on which a strong negative electric potential is applied. The potential together with the curvature of the needle induces a negative corona discharge, which yields free ions in the air. To numerically model the corona discharge phenomenon we use the resolved three species negative corona discharge model developed in (Johnson, et al., 2015) and (Wettervik, Johnson, Jakobsson, Mark, & Edelvik, 2015), which is based on modelling O_2^+ , O_2^- , e^- transport in the domain using their current densities created by their charge densities. Five reactions are included: ionization, attachment, and three recombination reactions.



Here M is an uncharged species participating in the reaction, mostly O_2 and N_2 . Denoting the rate coefficients k_i, k_a, k_{ep}, k_{np} , and the ion mobilities of the three species by μ_p, μ_n, μ_e , the equations for potential, ϕ , and charge densities, ρ_p, ρ_n, ρ_e , read:



$$\begin{aligned}-\Delta \phi &= (\rho_p + \rho_n + \rho_e)/(\epsilon_0) \\ \nabla \cdot (\mu_p \rho_p \nabla \phi) &= k_i \rho_e - k_{ep} \rho_e \rho_p - k_{np} \rho_n \rho_p \\ \nabla \cdot (\mu_n \rho_n \nabla \phi) &= k_a \rho_e - k_{np} \rho_n \rho_p \\ \nabla \cdot (\mu_e \rho_e \nabla \phi) &= (k_i - k_a) \rho_e - k_{ep} \rho_e \rho_p.\end{aligned}$$

The coefficients k_i , k_a , and μ_e are strongly dependent on the strength of the electric field, the other coefficients are treated as constants. The strength of the discharge is controlled by Townsend's second ionization coefficient, γ , which describes how often an extra electron is discharged from the cathode when it is hit by a positive ion. I.e., we set $\rho_e = \gamma \mu_p / \mu_e \rho_p$ on the cathode. The value of γ depends on the curvature and surface structure of the needle. We estimate its value from experimental current densities on the anode. The negative ion charge density is set to zero on the cathode and the positive ion density is set to 0 on the anode.

The resolved three species model simulations are performed in two dimensions, assuming rotational symmetry, and require a fine computational mesh. To couple the results with detailed coupled electrostatics – computational fluid dynamics – particle dynamics simulation resolving both the fluid, the electrostatics, and the trajectories of the particles, we reduce the three-species model to a one species model only containing negative ions. In the reduced models we set $\rho_e = 0$ and $\rho_p = 0$. Thus, the right-hand side of the equation for ρ_n is equal to zero. This means that we model conservation of current density. For the reduced model we introduce a scaling parameter for the number density of negative ions discharged from the cathode. This parameter is estimated from experimental values of the total current. I.e., we compute the resolved three-species electrostatics model once for a reference scenario and then for each specific detailed simulation we scale ρ_n from experiments to adapt the reduced model. A comparison of the current density below a needle with the one-species and three-species models is given in Figure 3.

The CFD model of the powder gun is based on a CAD model together with mass flow rates of fluid and paint powder. Powder is injected into the gun from a fluidized bed and is accelerated by the air. The mass flow rates are set on a control system for the gun. The air mass flow rate is set as an inlet velocity in the simulation. Electrostatics influence the fluid dynamics through the ion wind. We ignore, however, the influence of the fluid velocity on the electrostatics. The motivation is that the convective velocity is much lower than the drift velocity of ions ($= \mu_n E$), i.e., the convective contribution to the current density is negligible. This also allows us to only simulate the electrostatics once for each geometry. To model the fluid, we use the incompressible Reynolds' averaged Navier-Stokes equations with Menter's $k - \omega$ SST turbulence model (Menter, 1994) (Menter, Kuntz, & Langtry, 2003), which combines the $k - \epsilon$ turbulence model away from walls with the $k - \omega$ turbulence model close to walls and a viscous damping. The complete set of equations governing the fluid is:

$$\begin{aligned}\nabla \cdot \vec{u} &= 0 \\ \rho_f \frac{\partial \vec{u}}{\partial t} + \rho_f \vec{u} \cdot \nabla \vec{u} &= -\nabla p + (\mu + \mu_t) \Delta \vec{u} + \rho_n \vec{E} + \vec{F}_D \\ \rho_f \frac{\partial k}{\partial t} + \rho_f \vec{u} \cdot \nabla k &= P_k - \beta^* \omega k + (\mu + \sigma_k \mu_t) \Delta k \\ \rho_f \frac{\partial \omega}{\partial t} + \rho_f \vec{u} \cdot \nabla \omega &= \frac{\gamma}{\nu_t} P_\omega - \beta \omega^2 + (\mu + \sigma_\omega \mu_t) \Delta \omega + 2\rho_f (1 - F_1) \sigma_\omega \nabla k \cdot \nabla \omega \\ \mu_t &= \frac{\rho_f a_{1k}}{\max(a_{1\omega}, F_2 S)}\end{aligned}$$

Here $\rho_n E$ is the electrostatic force that yields the ion wind and F_D is the drag force from the particles. ρ_f is the fluid density, μ and μ_t are the molecular and turbulent viscosities, P_k and P_ω



are the production terms for turbulent kinetic energy and specific dissipation rate. F_1 and F_2 are interpolations controlling the blending of $k - \epsilon$ and $k - \omega$, and the viscous damping, respectively. The remaining constants are SST model parameters.

The third part of the detailed simulation is the particles. To model the particles, their size distribution is measured experimentally or given from the paint suppliers datasheet. In the simulation the particles are injected without charge based on their size distribution, defined using the volume fraction with respect to the total powder volume for a given set of particle diameter intervals. The computational particles are randomly generated from this size distribution, resampled in terms of total powder surface area. The number of particles is based on the total mass flow rate.

When the particles pass the corona needle, they are charged by ion bombardment, which is modeled by the Pauthenier-Moreau-Hanot equation (Pauthenier & Moreau-Hanot, 1932). The equation uses a local maximum charge, Q_{max} , and a relaxation time, τ , given by:

$$Q_{max} = \left(1 + \frac{\epsilon_r - 1}{\epsilon_r + 1}\right) 4\pi r^2 \epsilon_0 |\vec{E}|$$
$$\tau = \frac{4\epsilon_0}{\mu_n |\rho_n|}$$

where ϵ_r is the relative permittivity of the powder and r is the radius of the particle. The local charging is given by:

$$\frac{dQ}{dt} = \frac{Q_{max}}{\tau} \left(1 - \frac{Q}{Q_{max}}\right)^2, |Q| < |Q_{max}|$$

Charging primarily occurs close to the corona needle where the electric field and the ion current density are the strongest.

Particle dynamics is determined by the electrostatic force from the electric field, the drag force from the fluid, the gravity force, and a particle turbulence model. The particle turbulence model changes the local velocity field seen by a particle by taking the local turbulent kinetic energy into account. The fluctuating velocities seen by the particles are assumed to be isotropic, to be consistent with an isotropic turbulence model. The drag force is two-way coupled between the fluid and the particles. I.e., the particle trajectories are determined by:

$$\frac{dp}{dt} = F_D + \vec{g}(\rho_p - \rho_f) + q\vec{E}$$

where the drag coefficient and force are computed by the Schiller-Naumann model (Maxey & Riley, 1983):

$$C_d = \frac{24(1 + 0.15 * Re_p^{0.687})}{Re_p}, Re_p < 1000$$
$$0.44, Re_p > 1000$$

$$F_D = 0.75 C_d \frac{\rho_f}{\rho_p} \frac{m_p}{d_p} |\vec{u}_p - \vec{u}_f| (\vec{u}_p - \vec{u}_f)$$

The fluid velocity used for the drag force computation is perturbed by the turbulence to get a locally fluctuating velocity field. The strength of the perturbation is given by a random draw from a $N\left(0, \sqrt{\frac{2k}{3}}\right)$ distribution, the direction is given by a random point on a sphere. The



perturbation is updated based on an eddy-life time estimate. The resulting drag force is added symmetrically to the particles and the momentum equation.

The final part of our simulation framework is the thickness prediction simulation. It is performed based on the method described in (Edelvik, Mark, Karlsson, Johnson, & Carlson, 2017) updated with the corona discharge model, and the particle charging model. Another difference to the rotary bells described therein is that powder guns emit the paint as a flat stream. The paint injection model has been updated to reflect this. The coating is the point when the motion of the gun could be allowed to influence the simulations. It can either be that the gun is attached to a robot which is moving or that the objects are moving past a gun in a fixed position. For the powder coating simulation, the fluid fields: velocity, pressure, kinetic energy, specific dissipation, and eddy viscosity are read from a detailed simulation database and set in the vicinity of the gun. The particles are reinjected with their position, velocity and charge set from the detailed simulation. The reduced one species corona discharge model, however, is recomputed on the coating simulation grid. It is recomputed each time the geometry is updated, e.g., when the robot moves. To validate the coupling between the detailed simulation and the coating simulation we compare both the CEM and CFD solutions on several lines below the nozzle. It is also validated that the particle size distribution injected in the coating simulation is coinciding with the one injected in the detailed simulation.

The Navier-Stokes equations are discretized on a co-located Cartesian grid with the SIMPLE-C method (Van Doormaal & Raithby, 1984) using Rhie-Chow interpolation (Rhie & Chow, 1983) of the face velocities. Objects are added to the grid using the immersed boundary method (Mark & van Wachem, 2008) (Mark, Rundqvist, & Edelvik, 2011). The one-species electrostatics model is solved using a similar immersed boundary approach, but the potential and negative ion charge density are solved together in a Newton iteration scheme (Wettervik, Johnson, Jakobsson, Mark, & Edelvik, 2015). The three-species electrostatics model is discretized on a boundary conforming unstructured grid. For the three-species model the potential and the three species are solved iteratively using a segregated approach (Johnson, et al., 2015), a detailed description of the discretization is given in (Johnson, Röyttä, Mark, & Edelvik, 2016). The trajectories of the particles are integrated in time using the method described in (Edelvik, Mark, Karlsson, Johnson, & Carlson, 2017).

Model Validation and Results

In this section examples of the simulations performed to validate the models and coupling procedures, and to adjust model parameters are described: the three species corona model, the reduction of the three species corona model to a one species corona model, the corona scaling parameter, the charging of the particles in the detailed simulation, and the coupling of the detailed and the coating simulation for the electrostatics and the fluid dynamics models.

The validation of the three species model and its reduction to a one species model will be presented together, we therefore start by describing the reduction procedure. The corona discharge model reduction from three species to one species is performed on a sphere 1mm outside the needle, where the negative ion density is read. For the coating simulation a sphere with a radius of 2 cm is used. The sphere together with a CAD model of a gun at the needle is shown in Figure 1. The motivation why this is possible is that 1mm is sufficiently far away from the region where there is a significant number of free electrons in space. In Figure 2 the number densities of the three species are shown. From the figure one can determine the regions where ionization, attachment, and ion transport dominate. At a distance of 1 mm from the needle the negative ions dominate, and we are outside of the attachment region.

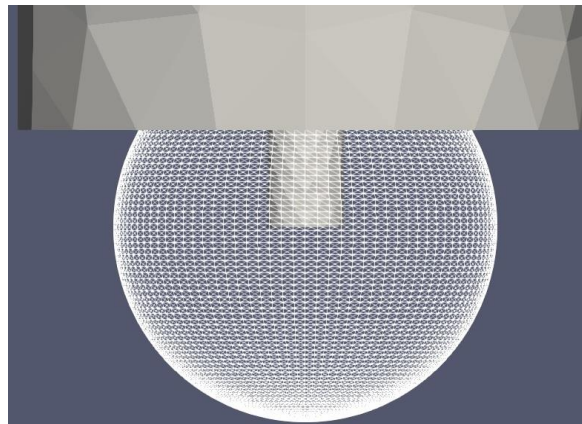


Figure 1: CAD model of the needle and the sphere where the species reduction is performed. The sphere is located 1 mm from the tip of the needle.

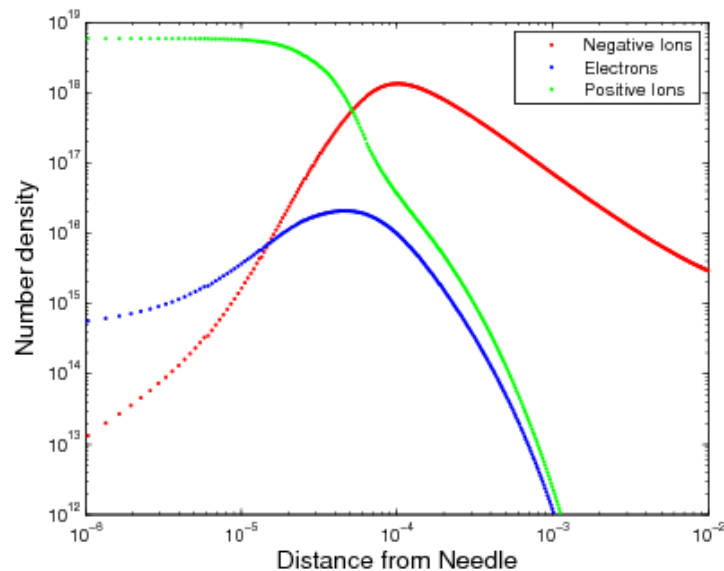


Figure 2: Number densities (particles / m³) of the three charged species close to the needle. At 1 mm the densities of electrons and positive ions are negligible. This is the motivation why the species reduction modelling can be performed. The negative ion density at 1 mm is sampled and reinjected for the detailed and coating simulations.

To validate the three species model itself, we perform measurements of current densities on a plate below a needle and compare the results with simulated current densities. The measurements are performed using the experimental method described in (Madani & Miller, 1998). The setup is also used as a final validation of the species reduction procedure. We compute the current densities with both models and compare them with the experiments. In the figures below we include the comparison for two voltages, -40 and -60 kV, and three needle to plate distances, 15, 20, and 25 cm. For the three species model the second Townsend ionization coefficient is used as a free parameter. We set it to $\gamma = 5 \times 10^{-2}$ and $\gamma = 10^{-8}$ for -40 kV and -60 kV, respectively. The three species model results are close to the experimental values. For the one species model the current densities match, except that the one-species model is not able to resolve the quick drop off at around 45°. The drop off is consistent



with the so-called Warburg law (Warburg, 1899), which states that the current density will depend on $\cos^5 \theta$, up to a threshold angle. The drop off is accurately predicted by the three species model.

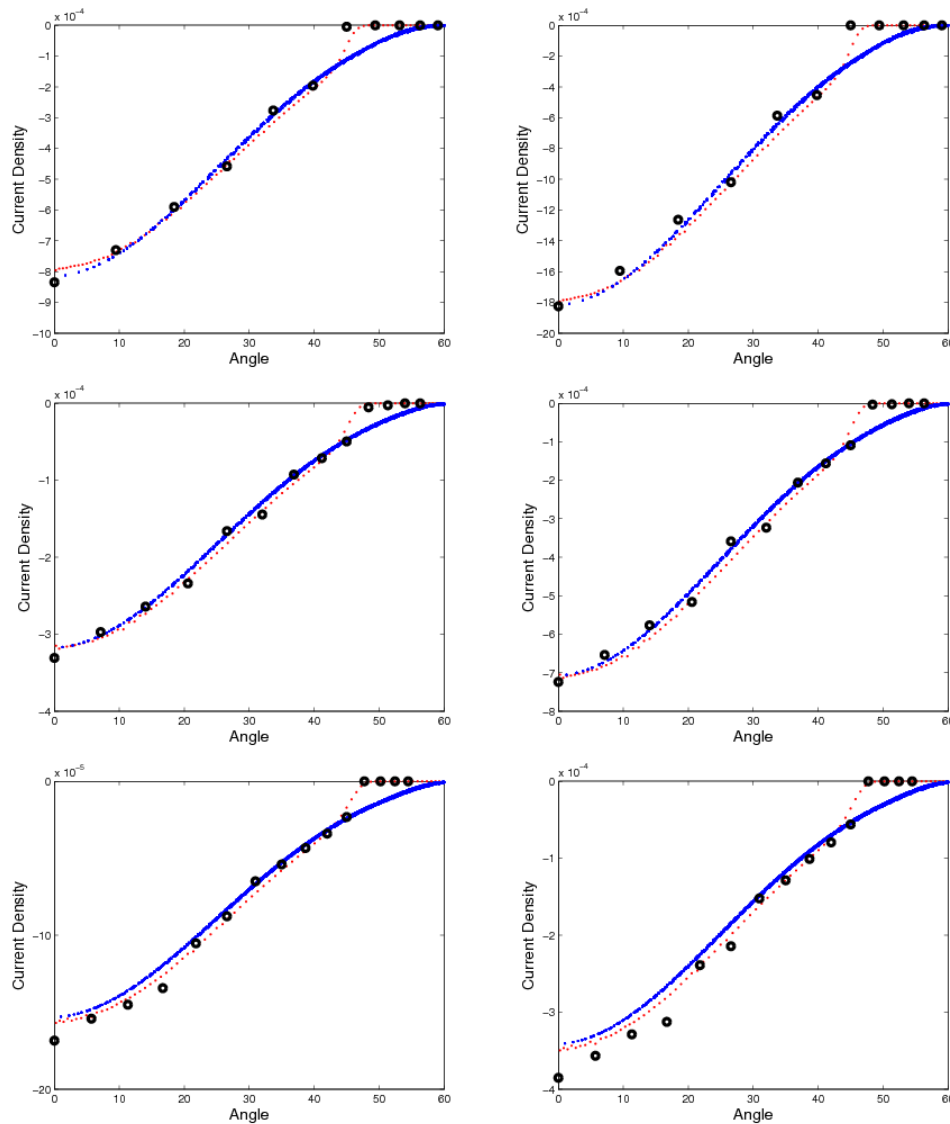


Figure 3: Current densities [A/m^2] on a flat plate 15, 20, and 25 cm below a corona discharge needle. The black circles are measurements, the red curves are simulations with the three species model, and the blue curves are simulations with the reduced one species model. The applied voltages are -40 kV (left) and -60 kV (right).

The detailed three species simulation was performed once for one needle. The reduced one species model is seen as fixed on the coupling sphere, except for a scaling of parameter, which is used to scale the charge density on the sphere. This scaling parameter depends on the distance



between the gun and the target object, but it is assumed to be constant for any effective voltage or current. The reduced solution on the sphere looks as follows:

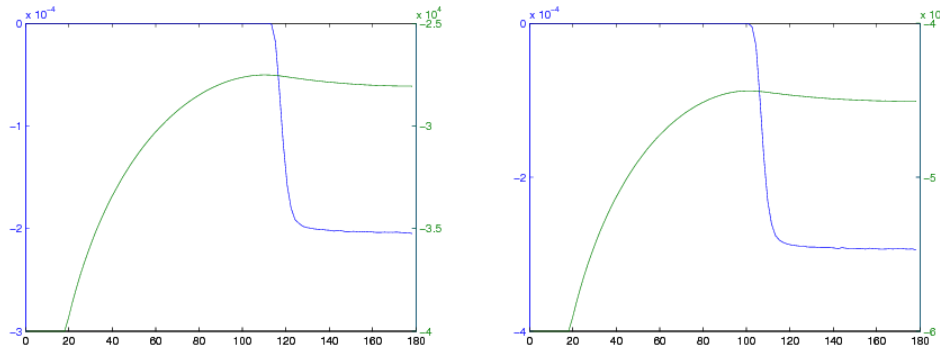


Figure 4: The values of ρ_n and ϕ for -40 and -60 kV on the coupling sphere 2 cm outside of needle. The green curve is the potential [V] and the blue curve is the charge density [C/m^3]. The angle is in degrees with the plate at 180.

For the remainder of this section, we will use an example of a powder gun to describe how the models are implemented and validated. The gun is a GEMA powder gun. Measurements on the gun have been performed by Fraunhofer IPA in a joint research project. The gun and its CAD model are shown below.



Figure 5: GEMA powder gun used for the experiments (left) and CAD model of the same gun (right)

To estimate how much the charge density, ρ_n , should be scaled for different distances, total current measurements have been performed at Fraunhofer IPA on a large aluminum plate. In particular, the current has been measured when the powder gun was placed at 12cm, 16cm and 20cm for different applied voltages. The experimental setup for these trials is shown in Figure 6. The current on the plate has been simulated for the same experimental settings using the one species model. The scaling parameters for the three distances have therefore been computed to minimize the difference between the measured and simulated currents for all the effective voltages in a least squares sense.

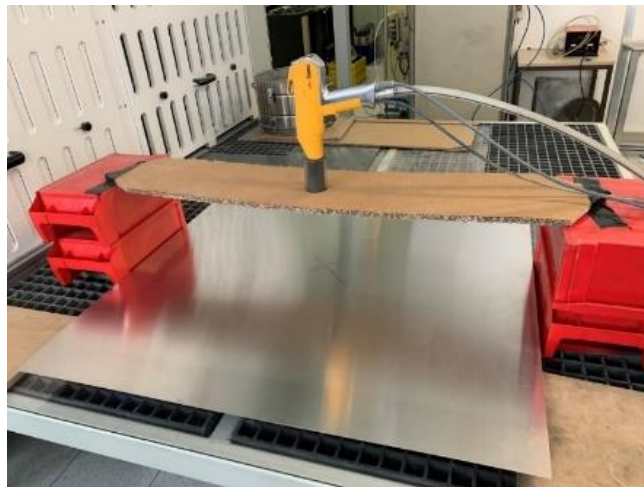


Figure 6: Experimental setup at Fraunhofer IPA to measure the total current below the gun for different needle to plate distances, and a range of potentials.

The negative ion density was therefore scaled accordingly to match the current as in the figure below, which shows excellent agreement between the experimental and simulated total currents.

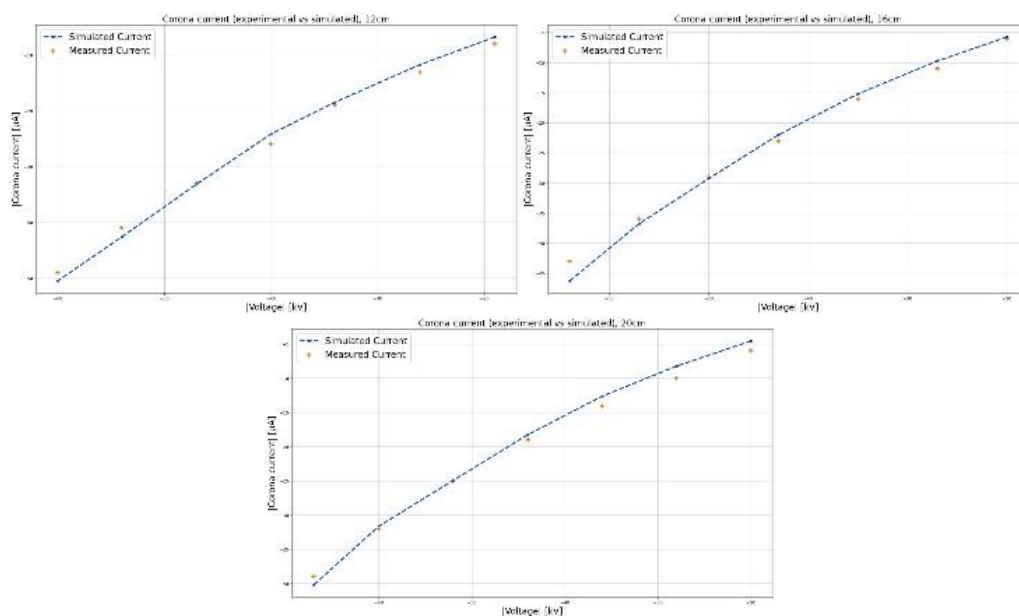


Figure 7: Total current (measured and simulated) for the spray gun at 12, 16, and 20 cm from the aluminum plate.

The corona discharge model, tuned to reproduce the experimental results, allows for the charging of the powder particles in our detailed simulation. When solving for the electrostatic quantities in the detailed simulation, both the current density and the maximum local charging according to the Pauthenier-Moreau-Hanot equation are estimated, see Figure 8.

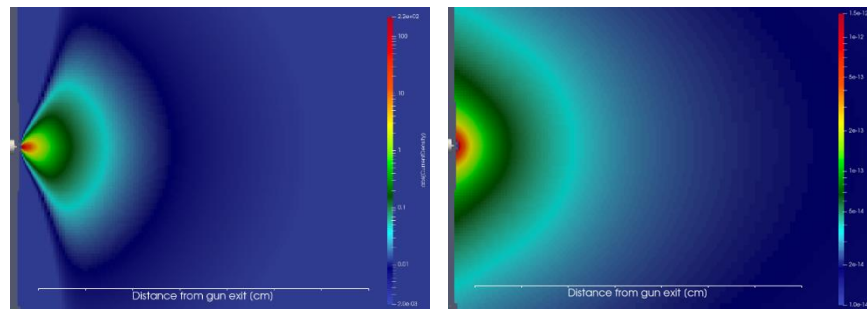


Figure 8: Simulated current density (left) and maximum local charge Q_{max} (right) below the needle.

These two quantities give an indication of where the particles get charged the most: in particular, we can conclude that most of the charging takes place within 3cm from the gun exit. Based on this observation, our coupling approach consists in extracting all the powder particles reaching a sampling cylinder placed at this distance with their velocity, charge, and volume values and reinjecting them randomly, unaltered, in the coating simulation. The powder particles sampled through this methodology can be analyzed with respect to their Charge (Figure 9) and Particle Size Distribution (Figure 13).

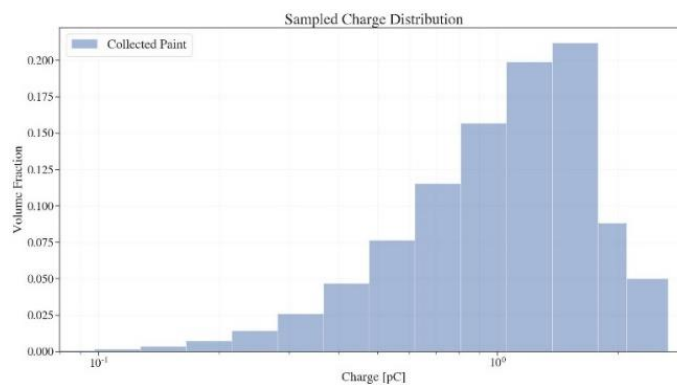


Figure 9: The charge distribution of the powder collected at the sampling cylinder with height 3cm and radius 5 cm.

To simulate the fluid flow inside and outside the gun the mass flow rate is specified at the inlet inside the gun. Flow is simulated in a large domain with total pressure condition on the domain boundary. The inlet turbulence intensity is set to 5 % and the eddy length to 10% of the inlet diameter. The simulation is run for long enough for the coupled fluid-particle simulation to stabilize. To ensure that there are no oscillations of the velocity and turbulence fields, the solutions are time-averaged.

The final model simplification in our approach is going from the detailed simulation to the coating simulation. The powder coating simulation has three components: the electrostatics, the particles, and the fluid. The electrostatics is recomputed but using a 2cm coupling sphere instead of a 1 mm coupling sphere for the boundary conditions for the potential and negative ion charge density. The particles exiting the sampling cylinder are reinjected as described above. The fluid solution from the detailed simulation is time-averaged for at least 0.02 s and sampled in a larger cylinder than the particles. It has a height of 5cm and radius 7cm. The velocity, turbulent kinetic energy, and specific dissipation rate are sampled inside the cylinder. The



averaged velocity field together with the particle and fluid sampling boxes are shown in Figure 10.

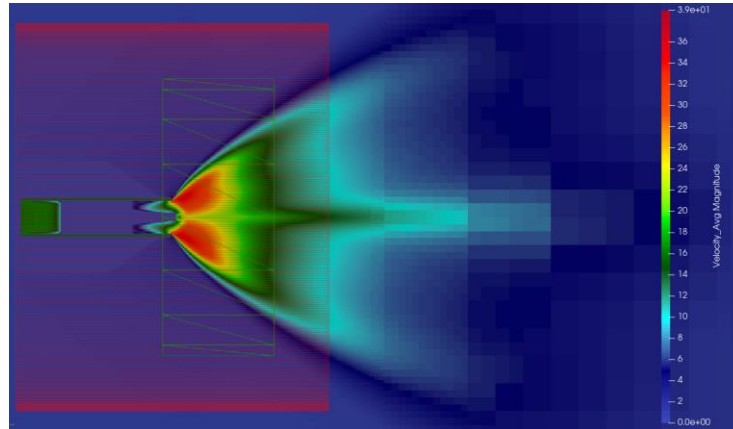


Figure 10: The stabilized averaged velocity field at the end of the detailed simulation. The red cylinder is the sampling cylinder for the fluid properties, and the green box is the sampling cylinder for the particles.

To check the modelling hypothesis that we can split the simulation in a detailed and a coating simulation, where the detailed simulation is stored, coarsened, and reimported to the coating simulation, we compare the solution for both the fluid and the electrostatics on several lines below the nozzle of the gun and parallel to the flat stream. On these lines we compare the velocities and current density profiles. As is seen in the two figures below, Figures 11 and 12, the coupling works well both in the electrostatics and the fluid dynamics domains. To ensure that the detailed simulation is run for a sufficiently long time not to influence the statistical properties of the size distribution of the paint particles, the particle size distributions injected to and collected from the detailed simulation are compared. As can be seen in the comparison in Figure 13, the particle size distribution is not affected by splitting the simulation into a detailed and a coating part.

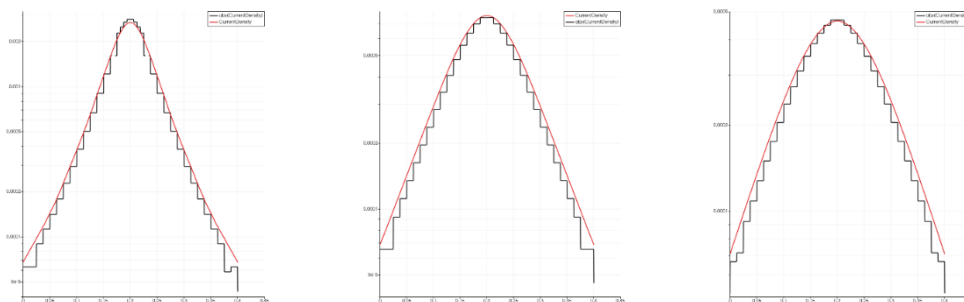


Figure 11: Current density at 5cm, 10cm, 15cm for detailed and paint thickness simulations.

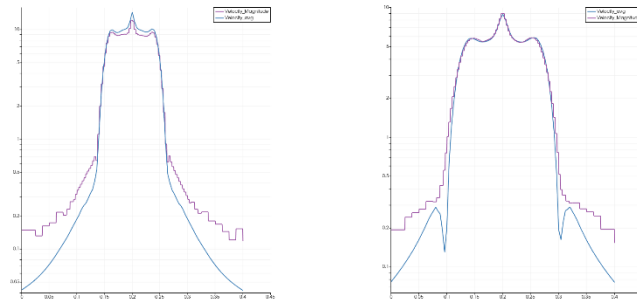


Figure 12: Axial velocity at 5 and 10cm distance for detailed and paint thickness simulations.

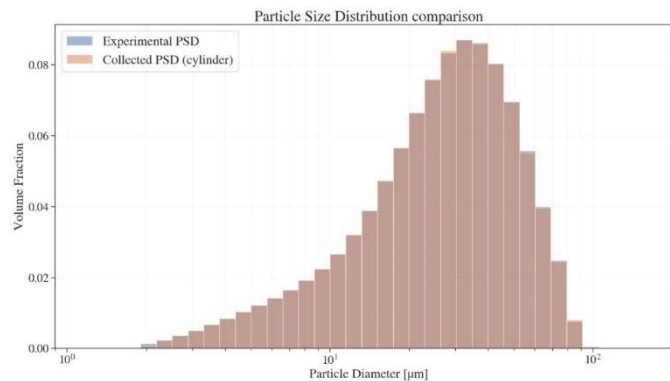


Figure 13: Particle Size Distribution preservation in the detailed simulation: experimental vs collected at cylinder.

This procedure with detailed simulation and sampling must be repeated, in principle, for the entire range of applied voltages, and fluid and particle mass flows in production, since changes in the corona discharge or either mass flow would affect the charge and velocity of the powder particles registered at the sampling cylinder. Within the range several values for each parameter should be simulated.

The models and methods presented here could be used to efficiently simulate powder coating. In the Quariapro project they have been used by the project partner IPS for simulation-based prediction of thickness profiles and size distributions.

Acknowledgement

This work was supported in part by the Swedish Governmental Agency for Innovation Systems, VINNOVA, through the project “Optimize powder coating quality and material efficiency by connecting process actuators and a digital twin”, Dnr 2019-05224.

References

Edelvik, F., Mark, A., Karlsson, N., Johnson, T., & Carlson, J. S. (2017). *Math-Based Algorithms and Software for Virtual Product Realization Implemented in*



- Automotive Paint Shops*. Retrieved 11 23, 2022, from https://link.springer.com/chapter/10.1007/978-3-319-63957-4_11
- Ingelsten, S., Mark, A., & Edelvik, F. (2019). A Lagrangian-Eulerian framework for simulation of transient viscoelastic fluid flow. *Journal of Non-Newtonian Fluid Mechanics*, 266, 20–32.
- Johnson, T., Jakobsson, S., Wettervik, B. S., Andersson, B. O., Mark, A., & Edelvik, F. (2015). A finite volume method for electrostatic three species negative corona discharge simulations with application to externally charged powder bells. *Journal of Electrostatics*, 74, 27-36. Retrieved 11 23, 2022, from <https://sciencedirect.com/science/article/pii/S0304388614001338>
- Johnson, T., Mark, A., Sandgren, N., Erhardsson, L., Sandgren, S., & Edelvik, F. (2022). Efficient Simulation of Convective Ovens in Automotive Paintshops. *Journal of Heat Transfer*, 144, 094501.
- Johnson, T., Røyttä, P., Mark, A., & Edelvik, F. (2016). Simulation of the spherical orientation probability distribution of paper fibers in an entire suspension using immersed boundary methods. *Journal of Non-Newtonian Fluid Mechanics*, 229, 1–7.
- Madani, M. R., & Miller, T. A. (1998). Current density distribution measurement of negative point-to-plane corona discharge. *IEEE Transactions on Instrumentation and Measurement*, 47, 907–913.
- Mark, A., & van Wachem, B. G. (2008). Derivation and validation of a novel implicit second-order accurate immersed boundary method. *Journal of Computational Physics*, 227, 6660–6680.
- Mark, A., Rundqvist, R., & Edelvik, F. (2011). Comparison between different immersed boundary conditions for simulation of complex fluid flows. *Fluid dynamics & materials processing*, 7, 241–258.
- Maxey, M. R., & Riley, J. J. (1983). Equation of motion for a small rigid sphere in a nonuniform flow. *The Physics of Fluids*, 26, 883–889.
- Menter, F. R. (1994). Two-equation eddy-viscosity turbulence models for engineering applications. *AIAA journal*, 32, 1598–1605.
- Menter, F. R., Kuntz, M., & Langtry, R. (2003). Ten years of industrial experience with the SST turbulence model. *Turbulence, heat and mass transfer*, 4, 625–632.
- Pauthenier, M., & Moreau-Hanot, M. (1932). La charge des particules sphériques dans un champ ionisé. *J. Phys. Radium*, 3, 590–613.
- Rhie, C. M., & Chow, W.-L. (1983). Numerical study of the turbulent flow past an airfoil with trailing edge separation. *AIAA journal*, 21, 1525–1532.



Van Doormaal, J. P., & Raithby, G. D. (1984). Enhancements of the SIMPLE method for predicting incompressible fluid flows. *Numerical heat transfer*, 7, 147–163.

Warburg, E. (1899). Ueber die spitzenentladung. *Annalen der Physik*, 303, 69–83.

Wettersvik, B. S., Johnson, T., Jakobsson, S., Mark, A., & Edelvik, F. (2015). A domain decomposition method for three species modeling of multi-electrode negative corona discharge – With applications to electrostatic precipitators. *Journal of Electrostatics*, 77, 139-146. Retrieved 11 23, 2022, from <https://sciencedirect.com/science/article/pii/S0304388615300346>